Ann. Phys. (Berlin) **525**, No. 1–2, 31–42 (2013) / DOI 10.1002/andp.201200204

annalen der physik

2D optical photon echo spectroscopy of a self-assembled quantum dot

Benjamin P. Fingerhut[1], *Marten Richter*[1,2], *Jun-Wei Luo*[3], *Alex Zunger*[4,*], *and Shaul Mukamel*[1,**]

Received 26 July 2012, revised 6 November 2012, accepted 8 November 2012
Published online 31 December 2012

Simulations of two dimensional coherent photon echo (2D-PE) spectra of self-assembled InAs/GaAs quantum dots (QD) in different charged states are presented revealing the coupling between the individual mono-exciton X^q transitions and contributions of bi-excitons XX^q. The information about the XX^q states is crucial for various application scenarios of QDs, like e.g. highly efficient solar cells. The simulations rely on a microscopic description of the electronic structure by high-level atomistic many-body pseudopotential calculations. It is shown that asymmetric diagonal peak shapes and double cross-peaks are the result of XX^q state contributions to the PE signal by analyzing the contributions of the individual pathways excited state emission, ground state bleach and excited state absorption. The results show that from the detuned X^q and XX^q contributions the bi-exciton binding energies of the XX^q manifold are revealed in 2D-PE signals.

1 Introduction

Matrix-embedded quantum dots (QD) offer the possibility to create a confined electronic space which can lead to the formation of bound bi-excitons from constituent single excitons. The existence of such exciton complexes has led to the proposal of numerous schemes for their utilization which ranges from next generation solar cells [1,2] (where multiple excitons are generated from a single electron-hole pair) [3–5] to quantum-computing [6–14] and entangled photon emitters (where a cascade decay of the bi- and mono-exciton creates phase correlated photon pairs) [11, 12, 14, 15].

Self-assembled dots represent a special case of QD where multi-excitons made of N_e electrons and N_h holes (including neutral $N_e = N_h$ as well as charged multi-excitons) decay radiatively, surviving many of the non-radiative decay channels that rapidly destroy multi-excitons in *colloidal* QDs [2, 16]. Only recently the internal structure of biexcitons in colloidal QD could be resolved [17, 18] laying the groundwork for the understanding of single self-assembled dots. In these *self-assembled* dots simple covalent semiconductors such as InAs are embedded seamlessly in a GaAs matrix [19, 20] forming artificial macro-molecules of molecular weight $\approx$ 1,000,000. As a result of the confinement of both InAs electrons and holes by the GaAs barrier, the electron Coulomb interaction and electron correlations are enhanced in such zero-dimensional (0D) QDs with respect to 2D quantum-wells and 1D quantum wires. The inherent many-body interactions in bi-exciton states can be identified by coherent optical non-linear techniques [21, 22].

Linear spectra of *self-assembled* QDs show in high-resolution a series of multi-exciton transition peaks observed with ultra high resolution with zero-phonon linewidth less than 10 μeV [23]. The absorption and emission spectra of single- and multi-excitons encode information about the Coulomb interactions between carriers, such as exchange and correlation effects and thus reveal many-particle physics in confined spaces [24]. Nevertheless information about homogeneous widths or many-body effects is not accessible by linear one dimensional (1D) techniques. Only a combination of 1D techniques (linear or non-linear in intensity) allows to access this information.

* Corresponding authors E-mail: alex.zunger@gmail.com
** E-mail: smukamel@uci.edu
[1] Department of Chemistry, University of California, Irvine, California, 92697-2025, USA
[2] Institut für Theoretische Physik, Nichtlineare Optik und Quantenelektronik, Technische Universität Berlin, Hardenbergstr. 36 10623, Berlin, Germany
[3] National Renewable Energy Laboratory, Golden, Colorado 80401, USA
[4] University of Colorado, Boulder, Colorado 80309, USA

In analogy to nuclear magnetic resonance (NMR) multidimensional spectroscopy can be extended to the optical wavelength regime. The mixing of multiple electromagnetic fields in a sample induces a signal field, which can be recorded in amplitude and phase by heterodyne detection. The excitonic response is affected by many-body effects [22] and characteristic dispersive line-shapes are induced in the non-linear response [25]. An additional powerful feature of coherent two dimensional (2D) optical spectroscopic techniques is the ability to reveal if individual transitions are coupled. The existence of peaks revealed in 1D techniques shows optical allowed transitions, but there is no way to determine if two transitions are fully independent or share a common state, i.e. are coupled. In 2D techniques independent transitions appear solely as diagonal peaks, whereas coupled transitions can show unique cross-peaks as off-diagonal features.

Coherent two dimensional (2D) optical spectroscopic techniques like photon echo (PE) spectroscopy or double quantum coherence (DQC) spectroscopy have been realized within the last decade [26,27] for quantum wells [22,28] and colloidal QD [29–33]. The population dynamics between quantum wells and colloidal QD has been measured [34]. Proposals for the measurement of interband coulomb interactions in colloidal QD have been published [35]. The 2D techniques can unfold complex and highly congested spectra by spreading them in two dimensions as is done in NMR [36–38]. Third order 2D spectra carry information about the mono- (X^q) and the bi-exciton (XX^q) manifold and couplings between X^q states beyond what can be inferred from linear spectroscopy (where $q = N_h - N_e$ denotes the charge of the QD): for example, the 2D-PE technique accesses the bi-exciton states XX^q states from mono-excitons X^q and reveals the coupling between mono-exciton transitions as cross-peaks. In coherent 2D third order PE experiments (as realized for colloidal QD [30–33] and quantum wells [22]) the QD interacts with a sequence of four (femtosecond and phase stable) laser pulses, the first two with wavevectors $\mathbf{k_1}$ and $\mathbf{k_2}$ excite the QD and create a population either in the mono-exciton manifold X^q or the ground state G^q; after a waiting time t_2 the third pulse with wavevector $\mathbf{k_3}$ creates either a $|G^q\rangle\langle X^q|$ coherence or accesses the bi-exciton manifold XX^q by creating a $|XX^q\rangle\langle X^q|$ coherence of the density matrix (see Fig. 1 (c)). The fourth pulse $\mathbf{k_4}$ is used for heterodyne detection which allows to record frequency, amplitude and phase information of the optical high frequency signal. The temporal control of the pulses and detection of the signal $S^{(3)}_{kl}$ in the direction $\mathbf{k_I} = -\mathbf{k_1} + \mathbf{k_2} + \mathbf{k_3}$ reduces the number of contributing pathways to an excited state emission (ESE), a ground state bleach (GSB) and an excited state absorption (ESA) type contribution compared to frequency domain techniques [23,36,39,40]. By varying the three time delays t_1, t_2, t_3 we obtain three dimensional projections of single- and multi-exciton correlations. These are usually displayed as two dimensional frequency-frequency correlation plots obtained by a double Fourier transform with respect to the first and third delays, holding the second fixed ($S^{(3)}_{kl}(\Omega_3, t_2, \Omega_1)$). Varying the t_2 delay allows insight into the dissipative populations dynamics within the X^q manifold. Due to the third interaction $\mathbf{k_3}$ the XX^q states are accessed from the X^q manifold along the Ω_3 axis [charge state q is the same in both mono-exciton and bi-exciton manifolds: $XX^0 = (2,2) \rightarrow X^0 = (1,1)$; $XX^+ = (3,2) \rightarrow X^+ = (2,1)$; $XX^- = (2,3) \rightarrow X^- = (1,2)$] showing the $XX^q \leftarrow X^q$ transitions due to ESA contributions to $S^{(3)}_{\mathbf{kl}}(\Omega_3, t_2, \Omega_1)$ [41]. This feature of 2D-PE reveals the XX^q states formed from pairs of electron-hole pairs not accessible by linear absorption spectroscopy. The $\mathbf{k_I}$ signal can be observed in bulk assemblies of QDs by simple looking in the direction $-\mathbf{k_1} + \mathbf{k_2} + \mathbf{k_3}$. Single dot signals are isotropic. Nevertheless the $\mathbf{k_I}$ signal can be extracted by using a wave guide geometry [23] and by repeating the experiment several times with different phases φ_l of the various pulses. This procedure, commonly used in 2D-NMR, is known as phase cycling. Alternatively, the detection of emission induced by a sequence of four phase controlled pulses yields similar information about quantum pathways [42–47] even in single molecules [48].

The 2D spectra provide detailed information that is successfully reproduced only by the microscopic theory. Here, we report the theoretical simulation of the 2D-PE signal of single InAs/GaAs QD with different charges. Such dots contain a few million atoms (dot + matrix) which requires special techniques to accurately determine the electronic structure of the QD. We use a high level atomistic many-body pseudopotential method [24, 49–53] for the description of the QD electronic structure. This allows to construct a microscopic excitonic Hamiltonian of X^q and the XX^q states which form the basis for the simulation of 2D-PE signals, without the need to adopt any site energies or couplings. We have recently reported that the DQC technique provides a sensitive tool for characterizing the charged state by strong signatures of Pauli-blocking due to partially occupied electron or hole states in the charged QD. The 2D-DQC signals revealed high order electron correlations allowing the analysis of XX^q states with regard to their constituent X^q manifold [54]. Here we analyze the PE signal with regard to signatures of XX^q states which are

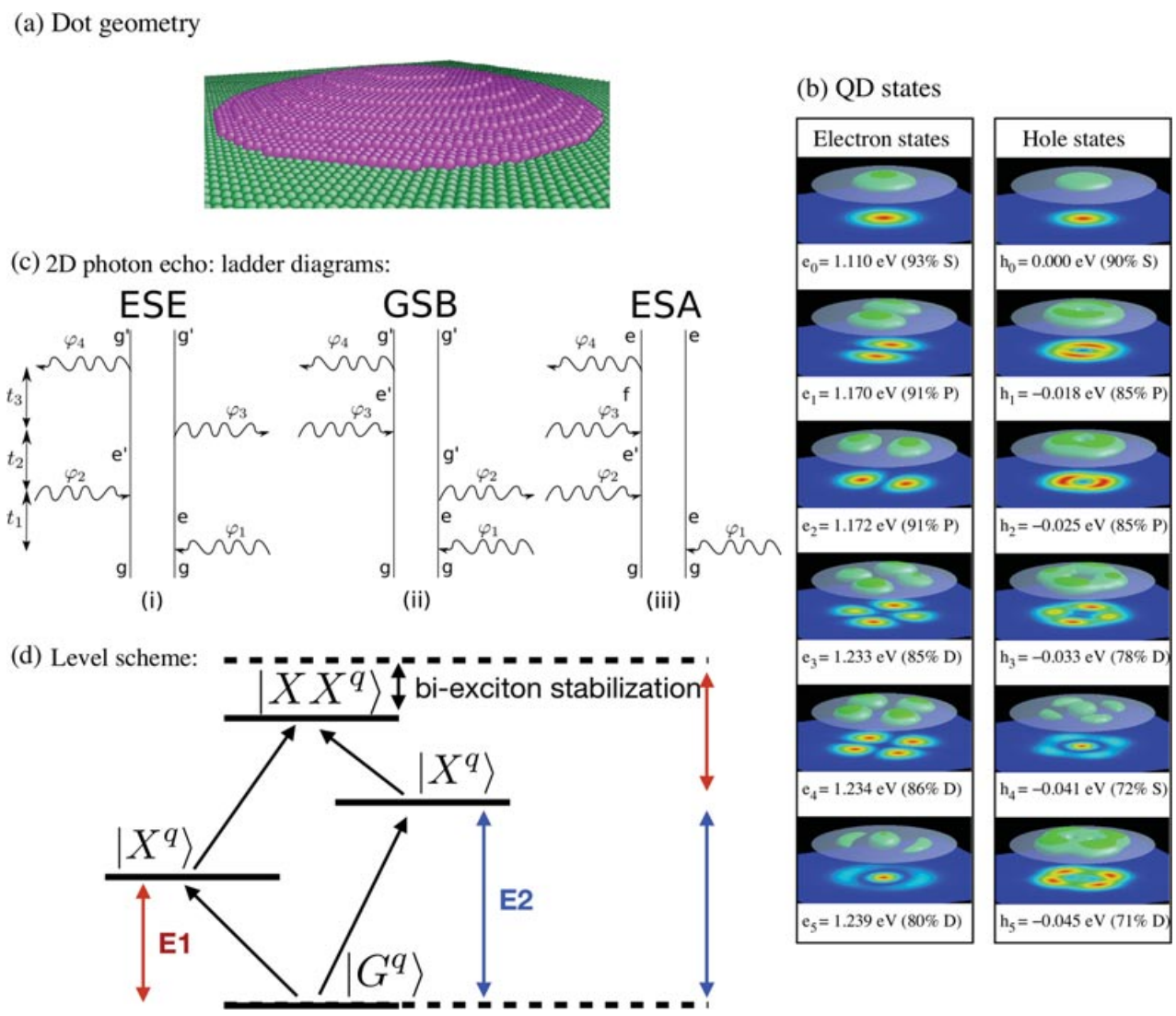

Figure 1 (online color at: www.ann-phys.org) (a) Schematic of a lens-shaped InAs dot with base of 25 nm and 2 nm heigh, sitting on one monolayer wetting layer, embedded in a GaAs matrix. The dot contains 41,776 atoms and the matrix contains 1,948,880 atoms. (b) Wavefunction square of six lowest energy single-particle electron states and six highest hole states. The percentage of its dominant orbital character (S, P and D) and its energy with respect to h_0 are given underneath the corresponding wavefunction plot. (c) Ladder diagrams excited state emission (ESE), ground state bleach (GSB) and excited state absorption (ESA) contributing to the 2D photon echo signal $S^{(3)}_{\boldsymbol{k_I}}$. (d) Schematic of the bi-exciton stabilization due to many-body effects in QD.

induced by excited state absorption (ESA) contributions to the signal. The bound biexcitons are energetically shifted compared to the bare two-exciton contributions due to the higher-order correlation effects in the QD. We show that specific cross-peaks originate from a common final XX^q state of the ESA contribution. The PE spectra are analyzed with regard to the interference between the constituent excited state emission (ESE), ground state bleach (GSB) and ESA contributions explaining the symmetric and asymmetric peak shapes of the PE signal.

2 Theoretical methods

The self-assembled QD is a lens-shaped InAs/GaAs QD with a circular base size of 25 nm diameter and 2 nm height sitting on one monolayers of "wetting layer" (Fig. 1 (a)). It contains 41,776 atoms and the matrix contains 1,948,880 atoms. The lattice mismatch between InAs and GaAs induces a build-in strain in the InAs/GaAs dot. An atomistic valence force field (VFF) model is used to relax the atomic position **r** in order to minimize the strain energy [52]. We consider

transition from the ground state manifold G^q [we considered neutral (no unpaired electron e or hole h (0,0)), negatively charged (an additional unpaired e in the QD (0,1)) and positively charged QD (an additional unpaired h in the QD (1,0))] into the single-exciton manifold X^q which generates an additional electron-hole pair in the respective charged QDs. The transitions are characterized by $G^0 = (0,0) \rightarrow X^0 = (1,1)$, $G^- = (0,1) \rightarrow X^- = (1,2)$, and $G^+ = (1,0) \rightarrow X^+ = (2,1)$, accordingly mono-exciton to bi-exciton transitions appear as $XX^0 = (2,2) \rightarrow X^0 = (1,1)$; $XX^+ = (3,2) \rightarrow X^+ = (2,1)$; $XX^- = (2,3) \rightarrow X^- = (1,2)$ (the charged state q is the same in both mono-exciton and bi-exciton manifolds).

2.1 Atomistic many body calculations

The details of the atomistic many-body pseudopotential method allowing to construct the excitonic Hamiltonian have been described elsewhere [24, 49–53]. In brief two steps are required to obtain the energies and respective transition matrix elements of X^q and XX^q states. In the *first step* we obtain single-particle approximated (without many-body interaction) energy levels $\{\epsilon_i\}$ and wavefunctions $\{\Phi_i(\mathbf{r})\}$ by solving the Schrödinger equation of crystal (dot+matrix) potential $V(\mathbf{r})$ in a linear combination of bulk bands (LCBB) method [51, 52]. The screened potential $V(\mathbf{r})$ is described as a superposition of overlapping atomic (pseudo) potentials centered at the atomic positions: $V(\mathbf{r}) = \sum_n \sum_\alpha \hat{v}_\alpha(\mathbf{r} - \mathbf{R}_n - \mathbf{d}_\alpha)$, where $\hat{v}_\alpha(\mathbf{r} - \mathbf{R}_n - \mathbf{d}_\alpha)$ pertains to atom type α at site $\mathbf{d}_\alpha$ in the nth primary cell $\mathbf{R}_n$. Thus it forces upon eigenstates the correct atomically-resolved symmetry [55–57]. The atomic potentials $\hat{v}_\alpha$ were empirically fit to experimental *bulk* quantities [52]. The approach cures the well-documented DFT bandgap and effective mass errors and captures the multi-band and inter-valley couplings. The wavefunctions are expanded by a set of plane-waves with a small energy cutoff $E_{cut} = 5$ Ry.

The *second step* is to calculate the many-body excitonic states $\{\epsilon_i, \Psi_i\}$ using a *screened* configuration interaction (CI) method [50] in a basis set of Slater determinants $\{\Phi_{v,c}\}$ constructed from 12 electron and 12 hole single-particle states (including spin) for the InAs/GaAs QD. The CI expansion takes into account all orbitals of the valence and conduction band states with S, P, and D orbital character of the envelope function (see Fig. 1 (c)). The convergence of the CI calculations, both in the energetic positions and intensity of the peaks has been investigated in [58, 59]. The electron correlations which play a predominant role in multi-dimensional quantum coherent spectra are taken into account by the configuration interaction. The interaction consists of electron-hole (e-h) Coulomb interaction (binding the e-h pair and thus forming the exciton) and e-h exchange interaction (splitting symmetry-different exciton states). The many-body exciton problem is set up in a basis set of Slater determinants as a CI expansion [50],

$$\left\langle \Phi_{v,c} \middle| H \middle| \Phi_{v',c'} \right\rangle = (\epsilon_c - \epsilon_v)\, \delta_{v,v'} \delta_{c,c'} - J_{vc,v'c'} + K_{vc,v'c'}, \qquad (1)$$

where J and K are the Coulomb and exchange integrals (expressions for J and K are given in the Supporting Information (SI)). Once the many-body wavefunctions of multi-excitons are solved from above equations, the dipole transition matrix elements will be readily obtained.

2.2 2D- photon echo (2D-PE) spectra

Using the CI wavefunctions and dipole transition matrix elements, we have constructed an effective three band exciton Hamiltonian, which is used for the calculation of the third order optical response: we considered neutral (no unpaired electron e or hole h (0,0)), negatively charged (an additional unpaired electron in the QD (0,1)) and positively charged QD (an additional unpaired hole in the QD (1,0)). The relevant exciton states form the ground state manifold $G^q = |q\rangle$, single-exciton manifold X^q [X^0 = (1,1) for the neutral QD, X^- = (1,2) for the negatively charged QD and X^+ = (2,1) for the positively charged QD], as well as the bi-exciton manifolds XX^q: XX^0 = (2,2) for the neutral QD, XX^- = (2,3) for the negatively charged QD and XX^+ = (3,2) for the positively charged QD. The total Hamiltonian has the form

$$H = H_0 + H_{eL} \qquad (2)$$

$$H_0 = \sum_{G^q} \varepsilon_{G^q} |G^q\rangle\langle G^q| + \sum_{X^q} \varepsilon_{X^q} |X^q\rangle\langle X^q| + \sum_{XX^q} \varepsilon_{XX^q} |XX^q\rangle\langle XX^q| \qquad (3)$$

$$H_{eL} = \sum_{G^q, X^q} E(t) \cdot \mu_{G^q, X^q} |G^q\rangle\langle X^q| + \sum_{X^q, XX^q} E(t) \cdot \mu_{X^q, XX^q} |X^q\rangle\langle XX^q| + c.c., \qquad (4)$$

where H_0 describes the isolated dot and H_{eL} is the interaction between quantum states of the isolated dot with

the optical field. In the case of negatively or positively charged QD the ground state manifold G^q has several states, in all simulations we assume, that the QD is initially in the lowest energy state G_0^q. The energy range of the X^q and XX^q manifold is chosen to cover the energy range of the $P_e - P_h$ channel (1.19 eV, compare Fig. 2) for $G^q \rightarrow X^q$ transitions and ≈ 2.31 eV for the $G^q - XX^q$ total energy range.

We simulate the 2D-photon-echo spectra solely on the basis of an atomistic Hamiltonian which involves hundreds of ground state to mono-exciton transitions and thousands of mono- to bi-exciton transitions with their respective dipole transition matrix elements. In the energy range considered the atomistic description of the QD yields 144 X^0 and 4356 XX^0 states, 500 X^+ and X^- and 1000 XX^+ and XX^- states which are explicitly considered in the Hamiltonian for the calculation of 2D-PE spectra. Together with the considered G^q manifold (12 states) this gives rise to $6 \cdot 10^7$ different transitions for the calculation of the 2D-PE signal. Hence the construction of a model Hamiltonian and the required couplings is avoided by the complete microscopic description of the QD. The sheer amount of states requires a huge computational effort where the complete 2D spectrum is calculated efficiently by distributing equally small tiles on a modern Linux cluster. Transitions which contribute dominantly to the linear absorption spectrum are given exemplarily in Tab. 1, the respective single-exciton and bi-exciton binding energies are given in the SI (SI-Tab. 1 and SI-Tab. 2). We note that only a few discrete states of the joint-density-of-states contribute to the linear absorption spectrum. Of all possible $G^q \rightarrow X^q$ transitions only a few posses substantial transitions strength due to the selection rules of QD transitions [60].

The 2D-PE spectra are calculated according to sum over state expressions of the third order response function (derived in detail in Ref. [37, 41]) which involve all possible transitions between the different blocks of the atomistic three band exciton Hamiltonian. Due to the temporal control of the pulses and phase matching conditions ($\mathbf{k_I} = -\mathbf{k_1} + \mathbf{k_2} + \mathbf{k_3}$) three ladder diagrams (depicted in Fig. 1 (c) contribute to the signal which parametrically depends on the delay times t_1, t_2 and t_3 between the incident pulses. Upon Fourier transformation of the first and third delay time t_1 and t_3 [41] the contributions to the PE-signal are given by:

$$\begin{aligned} S^{(3)}_{k_I}(\Omega_3, t_2, \Omega_1) = &+ S^{(ESE)}_{k_I,i}(\Omega_3, t_2, \Omega_1) \\ &+ S^{(GSB)}_{k_I,ii}(\Omega_3, t_2, \Omega_1) \\ &+ S^{(ESA)}_{k_I,iii}(\Omega_3, t_2, \Omega_1) \end{aligned} \tag{5}$$

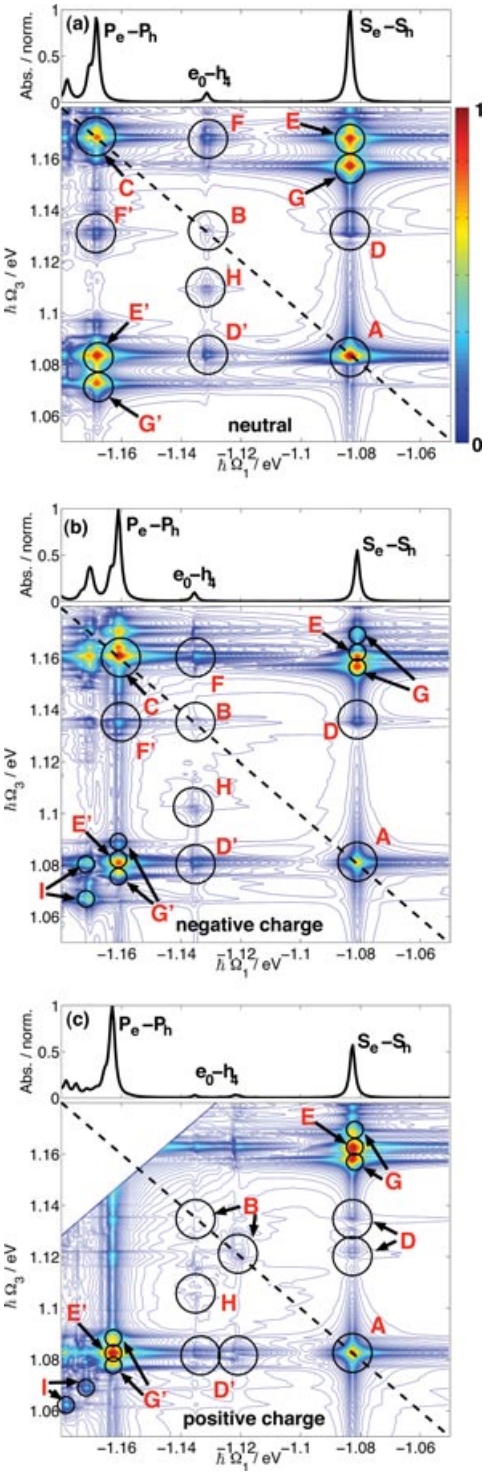

Figure 2 (online color at: www.ann-phys.org) 2D photon echo signal $S^{(3)}_{k_I}(\hbar\Omega_3, t_2, \hbar\Omega_1)$ (absolut value) of a neutral (a), negatively (b) and positively (c) charged QD ($t_2 = 0$): (top) linear absorption spectra of the transitions (a) $G^0 = (0,0) \rightarrow X^0 = (1,1)$, (b) $G^- = (0,1) \rightarrow X^- = (1,2)$, and (c) $G^+ = (1,0) \rightarrow X^+ = (2,1)$. The 2D-PE signals are depicted on a nonlinear scale, defined by eq. (10), the range of the signals is limited by the highest energy XX^q_{max} state.[1]

Table 1 Dominant $G^q \rightarrow X^q$ transitions contributing to the linear absorption spectrum of the neutral ($q = 0$), negatively charged ($q = -1$) and positively charged QD ($q = +1$): the number of the transition, transition energy ΔE (in eV), the absolute value of the transition matrix elements $|\mu|$ (in a.u.), character and dominant CI coefficients are given. The single particle states are given as wavefunction square in Fig. 1 (c).

q	#	ΔE [eV]	$\lvert\mu\rvert$ [a.u.]	character	CI conf.
q = 0					
	3	1.084	0.529	$S_e - S_h$	$e_0 - h_0$
	20	1.132	0.176	$e_0 - h_4$	$e_0 - h_4$
	35	1.168	0.482	$P_e - P_h$	$e_1 - h_1$
	40	1.171	0.296	$P_e - P_h$	$e_2 - h_1$
	48	1.178	0.280	$P_e - P_h$	$e_2 - h_2$
q = −1					
	2	1.081	0.287	$S_e - S_h$	$e_0 e_0 - h_0$
	10	1.136	0.195	$e_0 - h_4$	$e_0 e_0 - h_4$
	31	1.161	0.292	$P_e - P_h$	$e_0 e_1 - h_1$
	34	1.161	0.296	$P_e - P_h$	$e_0 e_1 - h_1$
	38	1.163	0.152	$P_e - P_h$	$e_0 e_2 - h_1$
	40	1.164	0.154	$P_e - P_h$	$e_0 e_2 - h_1$
	49	1.170	0.156	$P_e - P_h$	$e_0 e_2 - h_2$
	55	1.171	0.264	$P_e - P_h$	$e_0 e_2 - h_1$
q = +1					
	1	1.083	0.109	$S_e - S_h$	$e_0 - h_0 h_1$
	2	1.083	0.255	$S_e - S_h$	$e_0 - h_0 h_1$
	50	1.132	0.024	$e_0 - h_4$	$e_0 - h_0 h_4$
	58	1.135	0.053	$e_0 - h_4$	$e_0 - h_2 h_2$
	120	1.163	0.206	$P_e - P_h$	$e_1 - h_0 h_1$
	121	1.163	0.216	$P_e - P_h$	$e_1 - h_0 h_1$
	122	1.163	0.107	$P_e - P_h$	$e_1 - h_0 h_1$
	128	1.166	0.095	$P_e - P_h$	$e_0 - h_4 h_4$
	146	1.172	0.086	$P_e - P_h$	$e_2 - h_0 h_1$
	155	1.175	0.132	$P_e - P_h$	$e_2 - h_0 h_2$
	159	1.178	0.131	$P_e - P_h$	$e_1 - h_0 h_2$

These are of excited state emission (ESE), ground state bleach (GSB) and excite state absorption (ESA) type with the individual contributions given by:

$$S^{(3)}_{k_I,i}(\Omega_3, t_2, \Omega_1) = -\sum_{ee'g'} (\mu^*_{e'g'} \cdot E^*_s(\omega_{e'g'} - \omega_s))(\mu_{eg'} \cdot E_3(\omega_{eg'} - \Omega_3)) \times \frac{(\mu_{e'g_0} \cdot E_2(\omega_{e'g_0} - \omega_2))(\mu^*_{eg_0} \cdot E^*_1(\omega_{eg_0} - \Omega_1))}{\hbar^3(\Omega_3 - \xi_{e'g'})(\Omega_1 - \xi_{g_0 e})} \times e^{-\imath\xi_{e'e}t_2}, \quad (6)$$

$$S^{(3)}_{k_I,ii}(\Omega_3, t_2, \Omega_1) = -\sum_{ee'g'} (\mu^*_{e'g'} \cdot E^*_s(\omega_{e'g_0} - \omega_s))(\mu_{eg'} \cdot E_3(\omega_{eg'} - \Omega_3)) \times \frac{(\mu_{eg'} \cdot E_2(\omega_{eg'} - \omega_2))(\mu^*_{eg_0} \cdot E^*_1(\omega_{eg_0} - \Omega_1))}{\hbar^3(\Omega_3 - \xi_{e'g'})(\Omega_1 - \xi_{g_0 e})} \times e^{-\imath\xi_{g'g_0}t_2}, \quad (7)$$

$$S^{(3)}_{k_I,iii}(\Omega_3, t_2, \Omega_1) = \sum_{fee'} (\mu^*_{fe} \cdot E^*_s(\omega_{fe} - \omega_s))(\mu_{fe'} \cdot E_3(\omega_{fe'} - \Omega_3)) \times \frac{(\mu_{e'g_0} \cdot E_2(\omega_{e'g_0} - \omega_2))(\mu^*_{eg_0} \cdot E^*_1(\omega_{eg_0} - \Omega_1))}{\hbar^3(\Omega_3 - \xi_{fe})(\Omega_1 - \xi_{g_0 e})} \times e^{-\imath\xi_{e'e}t_2}, \quad (8)$$

with $\xi_{ij} = \omega_i - \omega_j - \imath\gamma$. Here g denotes the ground state manifold $|G^q\rangle$ of the QD, e denotes single-excitons $|X^q\rangle$ and f are bi-excitons $|XX^q\rangle$. All transitions are weight by the respective transition matrix elements μ_{G^q,X^q} and μ_{X^q,XX^q}. The pulse envelopes are given by

$$E(\omega) = \int \mathrm{d}t \exp(\imath\omega t) E(t) \quad (9)$$

From eqn. (6)–(8) and the diagrams depicted in Fig. 1 (c) we see that only the ESA contribution allows to access the bi-excitons manifold $|XX^q\rangle$. The ESE and GSB contributions show cross-peaks between coupled mono-excitons X^q along Ω_3 and Ω_1. Accordingly bi-exciton stabilization due to many-body effects in the QD (Fig. 1 (d)) is encoded in the $S^{(ESA)}_{k_I,iii}(\Omega_3, t_2, \Omega_1)$ contribution of the 2D-PE signal.

The 2D-PE signals are calculated for a delay time $t_2 = 0$ fs and are depicted on a non-linear scale

$$\mathrm{arcsinh}(\mathbb{S}) = \ln(\mathbb{S} + \sqrt{1 + \mathbb{S}^2}), \quad (10)$$

with $\mathbb{S} = 10\mathrm{abs}(S)/S^{(N)}$, where $S^{(N)}$ is a real normalization constant and S correspond to the 2D-PE signal $S^{(3)}_{k_I}$ on

the linear scale. This signal scale will interpolate between linear and logarithmic and highlights both weak features (e.g. subtle off-diagonal peaks) and strong features (e.g. diagonal and intense cross peaks) in a balanced fashion. Hence features which arise from weak transitions (e.g. $e_0 - h_4$ transitions) are presented together with the intense cross-peaks (e.g. $S_e - S_h$ $P_e - P_h$ cross-peaks) on a single scale (for details see Section 3).

The same phenomenological dephasing line width of $\gamma = 1$meV as used in the calculation of linear absorption spectroscopy is assumed for all exciton transitions, reflecting the width of sidebands of the QDs due to acoustical phonons [23, 61–64] and the similar radiative exciton lifetimes of single- and bi-excitons in single QD [65, 66]. In contrast to colloidal QDs, in single self-assembled QD the inhomogenous broadening is absent [61] and thus neglected in the calculations. If required it can be added subsequent to the calculation of the third order response function [67]. In all calculated spectra we assume that the bandwidth of the laser pulses is broader than the exciton band (exciton bandwidth from $S_e - S_h$ to $P_e - P_h$ is on the order of 100 meV). The broad bandwidth allows us to cover a large area of contributing exciton states and to reveal the relevant physical correlation between them in a single measurement.

3 Results

The solved single-particle QD states as the basis states of the CI expansion of X^q and XX^q states are shown in Fig. 1 (b). The ground electron state e_0 is S-like followed by two P-like and three D-like electron states (Fig. 1 (b), left). The S-like ground hole state h_0 is followed by two P-like and then one S-like state inserts into the three D-like states. It is obvious that the inter-orbital (e.g S-P) coupling is stronger in hole states than in electron states.

The linear absorption spectra for the neutral, negatively charged and positively charged QD (depicted in Fig. 2 (a)–(c), top) are calculated according to Fermi's golden rule, and involve the transitions $G^0 = (N_h = 0, N_e = 0) \rightarrow X^0 = (N_h = 1, N_e = 1)$ for the neutral QD, $G^- = (N_h = 0, N_e = 1) \rightarrow X^- = (N_h = 1, N_e = 2)$ for the negatively charged, and $G^+ = (N_h = 1, N_e = 0) \rightarrow X^+ = (N_h = 2, N_e = 1)$ for the positively charged QD. Earlier calculations of photoluminescence (PL) spectra for different exciton charges of this QD reproduce well the experimental measurement by Warburton's group [49]. The effects of variing dot sizes on the exciton binding energies has been investigated in detail in Ref. [58]. In the energy range $\hbar\omega = 1.05 - 1.18$ eV the linear absorption spectra show several resonances, which can be characterized by the angular momentum of the envelope wavefunctions of electron e_i and hole h_j of dominant orbital configuration $|e_i h_j\rangle$ of the many-body CI states as $e_i - h_j$ (Fig. 1 (b)). In the neutral QD (Fig. 2 (a), top)) the lowest energy exciton transition ($\hbar\omega = 1.08$eV) consists of the single-exciton $S_e - S_h$ channel, where both electron and hole states have spherical symmetry ($e_i - h_j = e_0 - h_0$). Due to the additional spin degree of freedom and the spin selection rule this transition is double degenerate. This channel corresponds to transitions between states with S-like wavefunctions (Fig. 1 (c), top). The exciton $P_e - P_h$ channel ($\hbar\omega = 1.16 - 1.18$ eV) consists of two orthogonal P-like states in both electron and hole (Fig. 1 (c), middle). Additionally two fold degeneracy due to the spin has to be taken into account. The transition $e_i - e_j = e_0 - h_4$; ($\hbar\omega = 1.13$eV) lies between the $S_e - S_h$ and $P_e - P_h$ states and posses only weak transition strength.

In both, the negatively charged QD [$G^- = (0,1) \rightarrow X^- = (1,2)$] (Fig. 2 (b)) and the positively charged QD [$G^+ = (1,0) \rightarrow X^+ = (2,1)$] (Fig. 2 (c)) the oscillator strength of the lowest energy $S_e - S_h$ transition is reduced compared to $P_e - P_h$. The number of possible transitions is reduced by a factor of 2 relative to the neutral QD. The additional electron in the negatively charged QD ($0h, 1e$) occupies one of the spin degenerate e_0 states, in the positively charged QD ($1h, 0e$) the additional hole occupies one of the two spin degenerate S-like h_0. The transitions of the $e_0 - h_4$ channel are shifted towards higher energies in the negatively charged QD ($\Delta\hbar\omega = 0.02$eV), in the positively charged QD the $e_0 - h_4$ transitions are split into two weak resonances (Fig. 2 (c)). The $P_e - P_h$ transitions in the neutral QD are split into several different states in the negatively and positively charged QD. Due to the odd population pattern of electron or hole states in the charged QDs the degeneracy of the exciton states is lifted and several distinct exciton states contribute to the absorption.

At the respective peak positions of the $S_e - S_h$, $e_0 - h_4$, and $P_e - P_h$ transitions in the linear spectra the diagonal peaks A, B and C appear in the photon echo $S^{(3)}_{\boldsymbol{k_I}}(\hbar\Omega_3, t_2 = 0, \hbar\Omega_1)$ signal of the neutral, the negatively charged and the positively charged QD (Fig. 2 (a)–(c), bottom) at $\hbar\Omega_3 = -\hbar\Omega_1 \approx 1.08$ eV, 1.13 eV and 1.16–1.17 eV, respectively[1]. Due to the high oscillator strength of the $S_e - S_e$ and $P_e - P_h$ transitions with the ground state G^q

[1] The spectral range of the coherent 2D spectra is limited by the highest energy two exciton state XX^q_{max}. Due to the high anharmonicity of the DOS only a limited number of XX^q states could be accessed in the CI calculations. The un-meaningful spectral region of the positively charged QD is whitened.

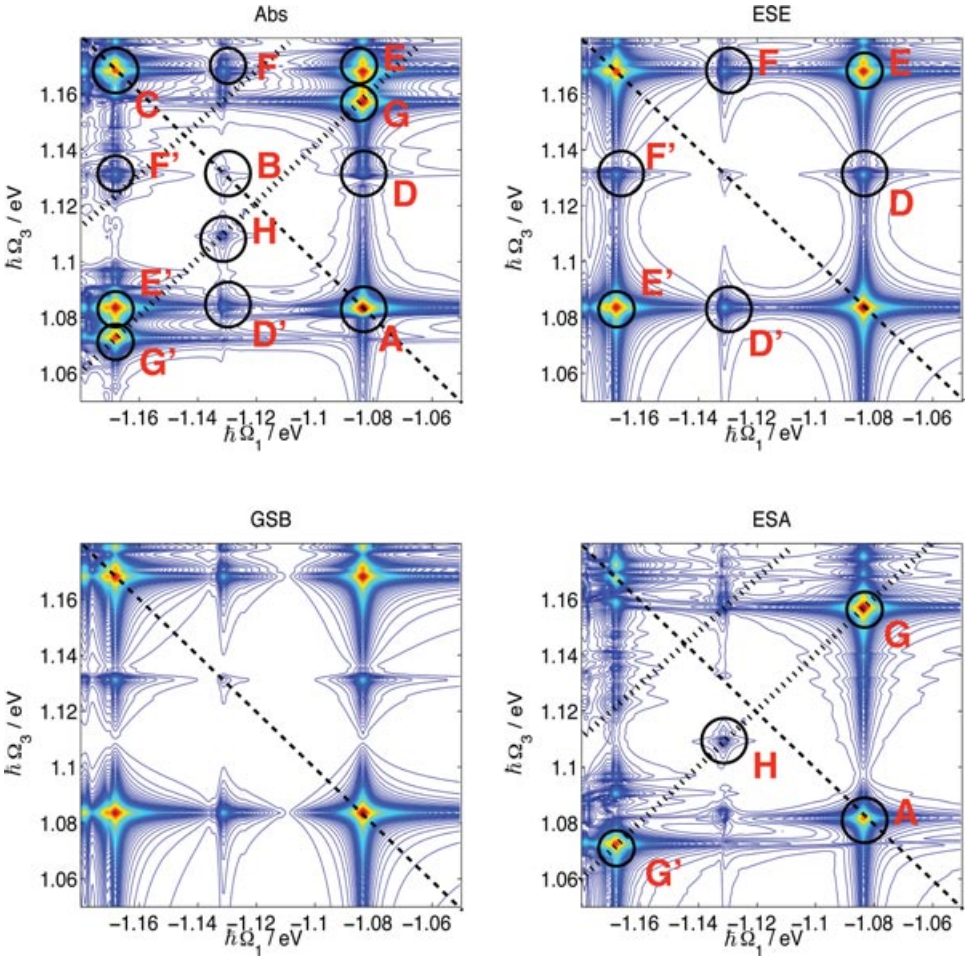

Figure 3 (online color at: www.ann-phys.org) 2D-Photon echo signal $S^{(3)}_{k_I}(\hbar\Omega_3, t_2, \hbar\Omega_1)$ of the neutral QD: the three ladder diagrams excited state emission (ESE), ground state bleach (GSB) and excited state absorption (ESA, compare Fig. 1) contribute to the total signal $S^{(3)}_{k_I}(\hbar\Omega_3, t_2, \hbar\Omega_1)$ (depicted as absolute value (Abs)). The signals are depicted on a nonlinear scale, defined by eq. (10). The colour scale is the same as in Fig. 2

the diagonal peaks A and C are more pronounced than the weak $e_0 - h_4$ transitions (peak B). It is noteworthy that the lowest energy diagonal peak A of the neutral QD ($S_e - S_h$ transition at $-\hbar\Omega_1 = \hbar\Omega_3 = 1.083$ eV, Fig. 2 (a)) shows a pronounced asymmetry which is not present for the charged QDs. All diagonal peaks arise from ground to single-exciton transitions ($X^q \leftarrow G^q$).

The most prominent off-diagonal feature (cross-peaks) of all QD is an intense multi peak structure at $-\hbar\Omega_1 \approx 1.08$ eV, $\hbar\Omega_3 \approx 1.16$ eV (for the upper diagonal peak) which arise from couplings of $S_e - S_h$ and $P_e - P_h$ transitions (cross-peaks E, E', G, G'). In the neutral QD (Fig. 2 (a)) we observe a clear doublet structure from the cross-peaks E and G, for the negatively and positively charged QD (Fig. 2 (b) and (c)) a more complex triplet is formed from the cross-peaks E and G. In the negatively charged QD additional cross-peaks arise from the couplings within the $P_e - P_h$ channel (for the positively QD, Fig. 2 bottom, the spectral range is limited in this region). Additional weaker cross-peaks occur at the resonances of the $S_e - S_h$ and $e_0 - h_4$ transitions (cross-peaks D, D', $-\hbar\Omega_1 \approx 1.08$ eV; $\hbar\Omega_3 \approx 1.13$ eV) and of the $e_0 - h_4$ and $P_e - P_h$ transitions (cross-peaks F, F', $-\hbar\Omega_1 \approx 1.13$ eV; $\hbar\Omega_3 \approx 1.17$ eV). We see that along the $\hbar\Omega_1$ axis all resonances can be assigned to transitions in the linear absorption spectrum, while along $\hbar\Omega_3$ resonances at new frequencies occur (cross-peaks G, G', H, $\hbar\Omega_3 \approx 1.07$ eV; $\hbar\Omega_3 \approx 1.158$ eV; $\hbar\Omega_3 \approx 1.115$ eV).

The origin of the multi peak structure of cross-peaks can be understood from the simplified level scheme of the QD single-excitons X^q and bi-excitons XX^q depicted in Fig. 1 (d). The ESE and GSB contribution to the 2D-PE signal $S^{(3)}_{k_I}(\hbar\Omega_3, t_2, \hbar\Omega_1)$ monitor $X^q \leftarrow G^q$ transitions and the coupling between single-excitons. The ESA

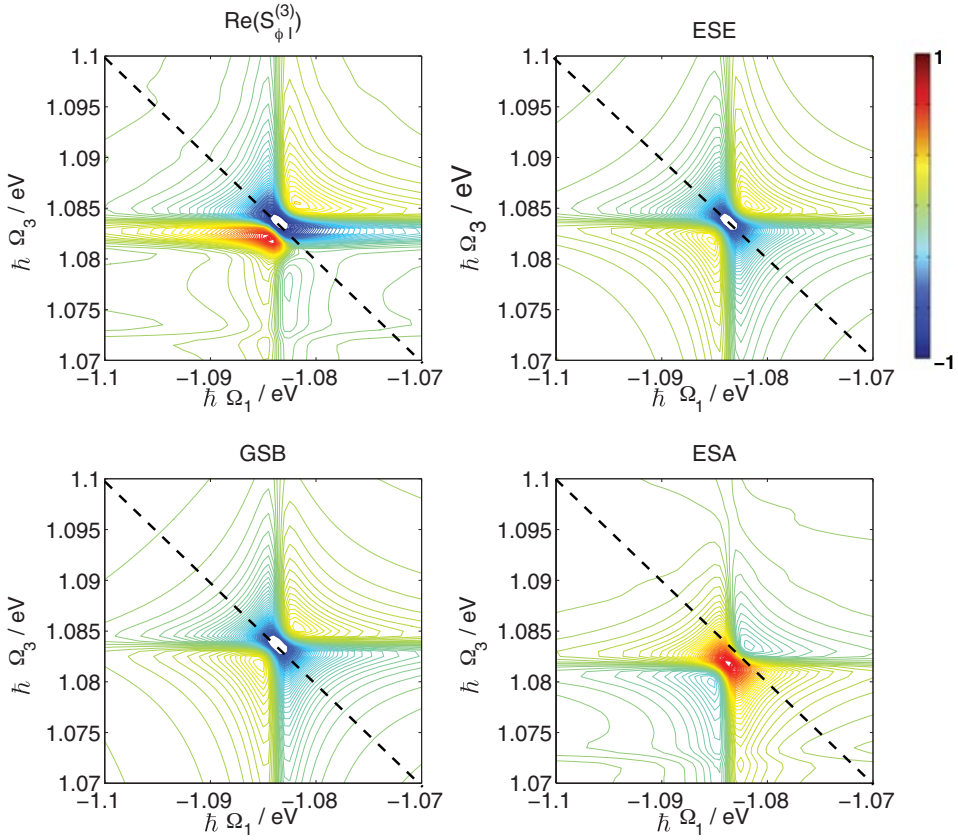

Figure 4 (online color at: www.ann-phys.org) Real part of the photon echo signal $S^{(3)}_{\boldsymbol{k}_I}(\hbar\Omega_3, t_2 = 0, \hbar\Omega_1)$ of the neutral QD: the asymmetric peak shape of the $S_e - S_h$ diagonal peak A arises from the interference of the pathways excited state emission (ESE), ground state bleach (GSB) and excited state absorption (ESA, compare Fig. 1). The signal is depicted on a nonlinear scale, defined by eq. (10).

contributions accesses the bi-exciton manifold showing $XX^q \leftarrow X^q$ transitions. If bi-exciton stabilization is absent the cross-peaks induced either from ESE and GSB or from ESA coincide and the different signs (see eqn. (6)–(8)) of the pathways leads to cancellation of crosspeak. Accordingly detuned $XX^q \leftarrow X^q$ transitions (from the fundamental $X^q \leftarrow G^q$) induce a double cross-peak in $S^{(3)}_{\boldsymbol{k}_I}(\hbar\Omega_3, t_2, \hbar\Omega_1)$ of the neutral QD (in the charged QD multi-peaks occur due to the presence of additional charged particles). The splitting of the double cross-peak directly reflects the bi-exciton stabilization due to many-body effects in the QD. The three pathways ESE, GSB and ESA (see Fig. 1 (d)), are depicted as absolute value for the neutral QD in Fig. 3 (the respective pathways of the charged QD are depicted in the SI). The analysis of the contributions of the ESE, GSB and ESA pathways to $S^{(3)}_{\boldsymbol{k}_I}(\hbar\Omega_3, t_2 = 0, \hbar\Omega_1)$ allows to trace the origin of the individual cross-peak resonances.

Contributions from the ESE and GSB diagram involve the ground to single-exciton transitions ($X^q \leftarrow G^q$), the bi-exciton manifold XX^q is not involved in these pathways. In both diagrams (Fig. 1 (c)) the system density matrix is in a $|G^q\rangle\langle X^q|$ or $|X'^q\rangle\langle G'^q|$ coherence during the time intervals t_1 and t_3. Upon Fourier transformation into the frequency domain $X^q \leftarrow G^q$ resonances appear along the $\hbar\Omega_1$ and $\hbar\Omega_3$ axis of both diagrams (note the symmetry of the ESE and GSB contributions in Fig. 3). The cross-peaks originating from the ESE and GSB diagrams are $S_e - S_h \leftrightarrow e_0 - h_4$ (cross-peaks D and D'), $S_e - S_h \leftrightarrow P_e - P_h$ (cross-peaks E and E') and $e_0 - h_4 \leftrightarrow P_e - P_h$ (cross-peaks F and F') showing the coupling between the fundamental $X^q \leftarrow G^q$ transitions of the linear absorption spectra.

Contributions to $S^{(3)}_{\boldsymbol{k}_I}(\hbar\Omega_3, t_2, \hbar\Omega_1)$ from the ESA diagram (Fig. 3, bottom right) additionally involve the bi-exciton manifold XX^q showing up from $XX^q \leftarrow X^q$ transitions. In the ESA diagram ((iii) in Fig. 1 (c)) the system density matrix is in a $|XX^q\rangle\langle X^q|$ coherence during t_3 and in a $|G^q\rangle\langle X^q|$ coherence during t_1. Accordingly $X^q \leftarrow G^q$ resonances are revealed along $\hbar\Omega_1$ and additional $XX^q \leftarrow X^q$ transitions appear along $\hbar\Omega_3$. The most intense ESA contribution are the cross-peaks G

and G' where the mono-excitons $S_e - S_h$ and $P_e - P_h$ are doorway states to a common bi-exciton state ($S_e - S_h \rightarrow XX^q$ and $P_e - P_h \rightarrow XX^q$). Due to the red detuned $X^q \rightarrow XX^q$ transitions (along $\hbar\Omega_3$) from the $G^q \rightarrow X^q$ fundamental transitions (along $\hbar\Omega_1$) cross-peaks with double peak structure appear in the total $S^{(3)}_{\boldsymbol{k}_I}(\hbar\Omega_3, t_2, \hbar\Omega_1)$ signal. The strong detuning directly reveals the bi-exciton binding energy in the QD due to many-body correlations. Similarly the cross-peak H shows the contribution of the mono-exciton doorway state $e_0 - h_4$ to a bi-exciton XX^q.

The nature of bi-exciton states XX^q is given by an anti-diagonal along $\hbar\Omega_3 - \hbar\Omega_1$. Along these lines cross peaks in the total spectrum $S^{(3)}_{\boldsymbol{k}_I}$ can be assigned to a common final state XX^q of the ESA contribution (see dotted lines in Fig. 3). For the G, H and G' cross-peaks we observe that all three contribute to a final XX^q state with strong multi-configuration character. The height of the cross-peaks, aligned along the diagonal, is a measure of the oscillator strength μ_{X^q, XX^q}. Setting $\hbar\Omega_3 = 0$ allows to deduce the optical dark ground state to bi-exciton $XX^q \leftarrow G^q$ transition energy. For this specific bi-exciton in the neutral QD we find $\hbar\omega_{XX^q \leftarrow G^q} = 2.24$ eV.

Similar to the neutral QD in the negatively charged QD (Fig. 2 (b)) the complex triplet structure of cross-peaks E, G, and I arises from the ESE/GSB pathways (cross-peak E) and ESA contributions (cross-peaks G and I) to the created bi-exciton XX^-. The splitting of the $P_e - P_h$ channel into distinct states in the charged QD due to the odd population pattern of electron or hole states leads to a more complex cross-peak pattern than in the neutral QD.

The asymmetry of the $S_e - S_h$ diagonal peak A of the neutral QD (Fig. 2 (a)) is a consequence of the ESA contribution to the signal. The signal intensity is defined by the interference of ESE, GSB, and ESA pathways on the amplitude level, which is depicted as real part in Fig. 4. The ESE and GSB interfere constructively and show resonances at the same $\hbar\Omega_1$ and $\hbar\Omega_3$ energy values. The ESA contribution is slightly shifted in its resonance frequency along the $\hbar\Omega_3$ axis towards lower values ($\Delta\hbar\Omega_3 =$ 2 meV) and introduces a pronounced asymmetry along the $\hbar\Omega_3$ axis in the real part of $Re(S^{(3)}_{\boldsymbol{k}_I})$ (Fig. 4, top left) as well as in the absolute value of the PE signal (Fig. 2 (a)). The additional electron in the negatively charged QD ($0h, 1e$) occupies one of the spin degenerate e_0 states, in the positively charged QD ($1h, 0e$) the additional hole occupies one of the two spin degenerate S-like h_0. The induced Pauli-blockade prevents the creation of bi-exciton $XX^{+/-}$ from the $S_e - S_h$ channel only. Thus in the negatively and positively charged QD the ESA pathway does not contribute to the $S_e - S_h$ diagonal peak A in the 2D-PE spectra resulting in a symmetric $S_e - S_h$ peak shape with the only contributions from ESE and GSB.

4 Summary and conclusions

We have reported two dimensional photon echo (2D-PE) spectra for QD's in different charged states. The cross-peaks in the 2D-PE signals directly reveal the coupling between $S_e - S_e$, $e_0 - h_4$, and $P_e - P_h$ transitions beyond what can be inferred from linear and non-linear 1D techniques. The contributions of the individual pathways excited state emission (ESE), ground state bleach (GSB) and excited state absorption (ESA) to the respective 2D spectra have been analyzed in detail and clear contributions of bi-exciton states (XX^q) to the signal have been revealed. The XX^q manifold leads to pronounced off-diagonal features in the 2D-PE spectra with multi peak structure arising from the ESA pathway. The ESA contributions appear as red detuned $XX^q \leftarrow X^q$ transitions along the $\hbar\Omega_3$ axis. These cross-peaks can serve as fingerprint to distinguish between the charged state of the QD. In the neutral QD a XX^0 resonance composed of $S_e - S_h$ channel is possible due to the spin degeneracy of the lowest energy X^0 $S_e - S_h$ transition. The ESA component to the 2D-PE spectra modulates the $S_e - S_h$ diagonal peak shape, resulting in a pronounced asymmetry of the peak. In the charged QDs the creation of the respective $S_e - S_h$ XX^q states is prevented due to Pauli-blocking.

In summary we have shown that the coherent third order technique 2D-PE allows to distinguish the quantum state of individual QD and to extract valuable information about the XX^q manifold, not accessible in linear absoprtion spectroscopy. Multi-dimensional coherent spectroscopy (or 2D phase modulated fluorescence variants) may serve as eminently suited tool to record the charging state of single QD devices in operation.

Acknowledgements. We gratefully acknowledge the support of the National Science Foundation through Grant No. CHE-1058791 and CHE-0840513, the Chemical Sciences, Geosciences and Biosciences Division, Office of Basic Energy Sciences, Office of Science, US Department of Energy. B. P. F. and M. R. gratefully acknowledge support from the Alexander-von-Humboldt Foundation through the Feodor-Lynen program. M. R. also acknowledges financial support from the Deutsche Forschungsgemeinschaft through the priority program "Ultrafast Nanooptics" SPP1391. The work did by J. W. L. and A. Z. was funded by the U.S. Department of Energy, Office of Science, Basic Energy Science, Materials Sciences and Engineering, under Contract No. DE-AC36-08GO28308 to NREL.

Key words. Self-assembled quantum dots, non-linear optical spectroscopy, many-body effects.

Supporting information for this article is available free of charge under http://dx.doi.org/10.1002/andp.201200204.

References

[1] O. E. Semonin, J. M. Luther, S. Choi, H. Y. Chen, J. Gao, A. J. Nozik, and M. C. Beard, Science **334**, 1530–1533 (2011).
[2] J. T. Stewart, L. A. Padilha, M. M. Qazilbash, J. M. Pietryga, A. G. Midgett, J. M. Luther, M. C. Beard, A. J. Nozik, and V. I. Klimov, Nano Lett. **12**, 622–628 (2012).
[3] A. Piryatinski and K. A. Velizhanin, J. Chem. Phys. **133**(8), 084508 (2010).
[4] P. Tyagi and P. Kambhampati, J. Chem. Phys. **134**(9), 094706 (2011).
[5] G. Nair, L. Y. Chang, S. M. Geyer, and M. G. Bawendi, Nano Lett. **11**(5), 2145–2151 (2011).
[6] D. Loss and D. P. DiVincenzo, Phys. Rev. A **57**, 120–126 (1998).
[7] P. Bhattacharya, S. Ghosh, and A. Stiff-Roberts, Ann. Rev. Mat. Res. **34**, 1–40 (2004).
[8] P. Michler, A. Kiraz, C. Becher, W. V. Schoenfeld, P. M. Petroff, L. Zhang, E. Hu, and A. Imamoglu, Science **290**, 2282–2285 (2000).
[9] A. J. Shields, Nature Photon. **1**, 215–223 (2007).
[10] C. Kindel, S. Kako, T. Kawano, H. Oishi, Y. Arakawa, G. Hönig, M. Winkelnkemper, A. Schliwa, A. Hoffmann, and D. Bimberg, Phys. Rev. B **81**, 241309 (2010).
[11] N. Akopian, N. H. Lindner, E. Poem, Y. Berlatzky, J. Avron, D. Gershoni, B. D. Gerardot, and P. M. Petroff, Phys. Rev. Lett. **96**, 130501 (2006).
[12] A. Schliwa, M. Winkelnkemper, A. Lochmann, E. Stock, and D. Bimberg, Phys. Rev. B **80**, 161307 (2009).
[13] F. Sotier, T. Thomay, T. Hanke, J. Korger, S. Mahapatra, A. Frey, K. Brunner, R. Bratschitsch, and A. Leitenstorfer, Nature Phys. **5**, 352–356 (2009).
[14] C. L. Salter, R. M. Stevenson, I. Farrer, C. A. Nicoll, D. A. Ritchie, and A. J. Shields, Nature **465**, 594–597 (2010).
[15] A. Mohan, M. Felici, P. Gallo, B. Dwir, A. Rudra, J. Faist, and E. Kapon, Nature Photon. **4**, 302–306 (2010).
[16] U. Woggon (ed.), Optical Properties of Semiconductor Quantum Dots (Springer Berlin, Berlin, 1997).
[17] P. Kambhampati, Acc. Chem. Res. **44**(1), 1–13 (2011).
[18] P. Kambhampati, J. Phys. Chem. Lett. **3**(9), 1182–1190 (2012).
[19] R. J. Warburton, C. Schaflein, D. Haft, F. Bickel, A. Lorke, K. Karrai, J. M. Garcia, W. Schoenfeld, and P. M. Petroff, Nature **405**, 926–929 (2000).
[20] M. Bayer, O. Stern, P. Hawrylak, S. Fafard, and A. Forchel, Nature **405**, 923–926 (2000).
[21] D. S. Chemla and J. Shah, Nature **411**(6837), 549–557 (2001).
[22] D. B. Turner and K. A. Nelson, Nature **466**(7310), 1089–1092 (2010).
[23] P. Borri, W. Langbein, S. Schneider, U. Woggon, R. L. Sellin, D. Ouyang, and D. Bimberg, Phys. Rev. Lett. **87**, 157401 (2001).
[24] V. Mlinar and A. Zunger, Phys. Rev. B **80**, 035328 (2009).
[25] S. T. Cundiff, T. Zhang, A. D. Bristow, D. Karaiskaj, and X. Dai, Acc. Chem. Res. **42**(9), 1423–1432 (2009).
[26] J. Kim, S. Mukamel, and G. D. Scholes, Acc. Chem. Res. **42**, 1375–1384 (2009).
[27] S. T. Cundiff, J. Opt. Soc. Am. B **29**, A69–A81 (2012).
[28] K. W. Stone, K. Gundogdu, D. B. Turner, X. Li, S. T. Cundiff, and K. A. Nelson, Science **324**, 1169–1173 (2009).
[29] L. A. Yurs, S. B. Block, A. V. Pakoulev, R. S. Selinsky, S. Jin, and J. Wright, J. Phys. Chem. C **115**, 22833–22844 (2011).
[30] C. Y. Wong and G. D. Scholes, J. Phys. Chem. A **115**(16), 3797–3806 (2011).
[31] C. Y. Wong and G. D. Scholes, J. Lumin. **131**(3), 366–374 (2011).
[32] E. Harel, S. M. Rupich, R. D. Schaller, D. V. Talapin, and G. S. Engel, Phys. Rev. B **86**(Aug), 075412 (2012).
[33] D. B. Turner, Y. Hassan, and G. D. Scholes, Nano Lett. **12**(2), 880–886 (2012).
[34] G. Moody, M. E. Siemens, A. D. Bristow, X. Dai, A. S. Bracker, D. Gammon, and S. T. Cundiff, Phys. Rev. B **83**, 245316 (2011).
[35] K. A. Velizhanin and A. Piryatinski, J. Phys. Chem. B **115**(18), 5372–5382 (2011).
[36] C. Scheurer and S. Mukamel, J. Chem. Phys. **115**, 4989–5004 (2001).
[37] S. Mukamel, R. Oszwaldowski, and D. Abramavicius, Phys. Rev. B **75**, 245305 (2007).
[38] S. Mukamel, R. Oszwaldowski, and L. Yang, J. Chem. Phys. **127**, 221105 (2007).
[39] P. Tian, D. Keusters, Y. Suzaki, and W. S. Warren, Science **300**, 1553–1555 (2003).
[40] M. F. Gelin, D. Egorova, and W. Domcke, Acc. Chem. Res. **42**, 1290–1298 (2009).
[41] D. Abramavicius, B. Palmieri, D. V. Voronine, F. Šanda, and S. Mukamel, Chem. Rev. **109**, 2350–2408 (2009).
[42] M. Cho, N. F. Scherer, G. R. Fleming, and S. Mukamel, J. Chem. Phys. **96**, 5618–5629 (1992).
[43] T. J. Dunn, I. A. Walmsley, and S. Mukamel, Phys. Rev. Lett. **74**, 884–887 (1995).
[44] P. F. Tekavec, G. A. Lott, and A. H. Marcus, J. Chem. Phys. **127**, 214307 (2007).
[45] J. A. Cina, Annu. Rev. Phys. Chem. **59**, 319–342 (2008).
[46] G. A. Lott, A. Perdomo-Ortiz, J. K. Utterback, A. Aspuru-Guzik, and A. H. Marcus, Proc. Nat. Acad. Sci. USA **108**, 16521–16526 (2011).
[47] S. Mukamel and M. Richter, Phys. Rev. A **83**, 013815 (2011).
[48] D. Brinks, F. D. Stefani, F. Kulzer, R. Hildner, T. H. Taminiau, Y. Avlasevich, K. Müllen, and N. F. van Hulst, Nature **465**, 905–908 (2010).
[49] M. Ediger, G. Bester, A. Badolato, P. M. Petroff, K. Karrai, A. Zunger, and R. J. Warburton, Nature Phys. **3**, 774–779 (2007).

[50] A. Franceschetti, H. Fu, L. W. Wang, and A. Zunger, Phys. Rev. B **60**, 1819–1829 (1999).
[51] L. W. Wang and A. Zunger, Phys. Rev. B **59**, 15806–15818 (1999).
[52] A. J. Williamson, L. W. Wang, and A. Zunger, Phys. Rev. B **62**, 12963–12977 (2000).
[53] G. Bester, S. Nair, and A. Zunger, Phys. Rev. B **67**, 161306 (2003).
[54] B. P. Fingerhut, M. Richter, J. W. Luo, A. Zunger, and S. Mukamel, Phys. Rev. B **86**, 235303 (2012).
[55] J. W. Luo, L. Zhang, and A. Zunger, Phys. Rev. B **84**, 121303 (2011).
[56] J. W. Luo, A. N. Chantis, M. van Schilfgaarde, G. Bester, and A. Zunger, Phys. Rev. Lett. **104**, 066405 (2010).
[57] J. W. Luo, G. Bester, and A. Zunger, Phys. Rev. Lett. **102**, 056405 (2009).
[58] J. Shumway, A. Franceschetti, and A. Zunger, Phys. Rev. B **63**, 155316 (2001).
[59] V. Mlinar, A. Franceschetti, and A. Zunger, Phys. Rev. B **79**, 121307 (2009).
[60] V. Mlinar and A. Zunger, Phys. Rev. B **80**, 205311 (2009).
[61] B. Krummheuer, V. M. Axt, and T. Kuhn, Phys. Rev. B **65**, 195313 (2002).
[62] J. Förstner, C. Weber, J. Danckwerts, and A. Knorr, Phys. Status Solidi B **238**, 419–422 (2003).
[63] B. Krummheuer, V. M. Axt, T. Kuhn, I. D'Amico, and F. Rossi, Phys. Rev. B **71**, 235329 (2005).
[64] E. Stock, M. R. Dachner, T. Warming, A. Schliwa, A. Lochmann, A. Hoffmann, A. I. Toropov, A. K. Bakarov, I. A. Derebezov, M. Richter, V. A. Haisler, A. Knorr, and D. Bimberg, Phys. Rev. B **83**, 041304 (2011).
[65] G. Bacher, R. Weigand, J. Seufert, V. D. Kulakovskii, N. A. Gippius, A. Forchel, K. Leonardi, and D. Hommel, Phys. Rev. Lett. **83**, 4417–4420 (1999).
[66] C. Santori, G. S. Solomon, M. Pelton, and Y. Yamamoto, Phys. Rev. B **65**, 073310 (2002).
[67] D. Abramavicius and S. Mukamel, J. Chem. Phys. **133**, 184501 (2010).